

An Autonomous Swarm of Micro Flying Robots with Range-based Relative Localization

Shushuai Li, Mario Coppola, Christophe De Wagter and Guido C. H. E. de Croon

Abstract—Accurate relative localization is an important requirement for a swarm of robots, especially when performing a cooperative task. This paper presents an autonomous multi-robot relative positioning technique. An Extended Kalman filter (EKF) uses onboard sensing of velocity, yaw rate, and height as inputs, and then estimates the relative position of other robots by fusing these quantities with ranging measurements obtained from onboard ultra wide-band (UWB). Specifically, innovations involve fast ranging communication (333Hz for 2 robots), an automatic initialization procedure, proofs and demonstrations of consistent estimation convergence under control commands such as formation flight. Simulations concisely show the high precision, efficiency, and stability of the proposed localization method. Real-world experiments are conducted on a team of 5 Crazyflie2 quadrotors, demonstrating autonomous formation flight and coordinated flight through a window. All results indicate the effectiveness of the proposed relative positioning method for multi-robot systems. Video and code can be found at <https://shushuai3.github.io/autonomous-swarm/>

I. INTRODUCTION

Aerial multi-robot systems have been widely studied recently because of their advantages, such as: efficiency of parallel task processing [1], the cooperative ability of performing team missions [2], [3], and the ability of smaller drones to operate safely in confined spaces and near humans [4], [5]. These systems require the relative position of peer robots so as to enable intra-swarm collision avoidance, coordination, and more. Therefore, the development of accurate relative localization technologies is an important challenge to be solved.

One solution to the above is to use external positioning systems. For example, there are many indoor examples of teams of multiple quadrotors which are localized with a motion capture system [1], [6], [7]. In [8], 30 drones exhibit outdoor flocking behaviour by relying on a Global Navigation Satellite System (GNSS) for positioning. Global positioning system (GPS) is employed for formation control of multiple quadrotors in [9]. Alternatively, fixed wireless UWB beacons are another external system that can provide positions for multiple robots [10]. All these systems have been instrumental in illustrating the potential of drone swarms, of how they can pass through a window together [6] or how they can perform beautiful choreographies [7]. However, the availability of the aforementioned systems is too limited to allow for autonomous flight in unknown and GPS-denied environments.

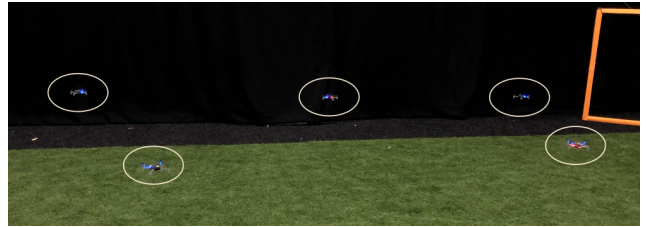


Fig. 1. The autonomous flight of multiple Crazyflie2 quadrotors without GPS or motion capture system, fully based on relative localization using onboard sensing information of velocity, yaw rate, height and ranging measurements between any two robots.

Other techniques allow for onboard relative localization between multiple robots. Several implementations are based on vision. To simplify the task, [11] and [12] designed a simple pattern that could be detected by a monocular camera to calculate the relative position of other vehicles. In [3], a follower tracks an April Tag mounted on the leader, enabling the duo to perform a collaborative task. Some more recent techniques involve detecting active LED tags [13] and ultraviolet light [14]. Vision-based methods have intrinsic scalability, i.e., no limitation on the number of robots. However, these vision-based methods are sensitive to the visibility of the markers or robots, which depends on aspects such as the size of the marker or robots, and the field of view of the robots' cameras. Markerless detection requires heavy onboard computation such as [15] and [16], and a large localization error occurs when inter-robot distance getting far. This creates an important limitation for its application in tiny exploration robots. Another vision-based strategy is not to have the robots detect and localize each other, but to perform a formation flight based on visual-inertial odometry [17]. However, this system requires a known initial position of each drone, and can drift over time, potentially leading to losing formation or even collisions.

Other studies have also seen the exploration of alternative technologies such as sound-based relative localization [18], or infra-red relative localization [19], although these require larger sensor arrays to be mounted on the robot, which is impractical for low-cost micro multiple robots.

As an alternative approach, relative localization based on wireless communication between drones has the advantages of being light-weight and omnidirectional. Here, the robots use antennas to exchange sensory information (e.g., velocity, yaw rate, height) and combine these with relative range measurements obtained from the antennas. This method was explored by [20] and [21], [22] for aerial robots. These studies required the knowledge of a common orientation. This

All authors are with Faculty of Aerospace Engineering, Delft University of Technology, 2629 HS Delft, The Netherlands (e-mail: s.li-6@tudelft.nl; m.coppola@tudelft.nl; c.deWagter@tudelft.nl; g.c.h.e.decroon@tudelft.nl)

limitation was overcome in [23], demonstrating a system of 3 drones in leader-follower flight. However, all the aforementioned works lack an estimation convergence analysis for large unknown initial state errors and for unobservable control commands. In addition, their works have not been implemented on tiny drones, neither with a clearly defined initialization procedure for the northless case.

To solve these problems, this paper proposes an automatic initialization procedure such that the relative estimation error converges even with large unknown initial positions of all robots. In addition, the relative estimation is proven to remain converged even with unobservable states caused by some system inputs. These two aspects confer fully autonomous and robust localization to real-world multiple robots. The overall localization system has many advantages over recent research, such as light and low-cost estimation compared to visual-inertial UWB fusion [24]; and higher speed (333Hz) ranging communication than that in previous studies, e.g., 40Hz [25] and 10Hz [26]. These fast ranging measurements enhance the estimation update speed such that the localization precision can be greatly improved in larger teams. Specifically, this work has the following contributions:

- An autonomous relative localization implemented on multiple *nano* (33 grams) flying robots with fully onboard perception.
- Localization *convergence analysis* for both random initialization maneuvers and unobservable maneuvers.
- *Robust* and *fast* communication rules that allow for a high-speed estimation update.
- Automatic *initialization procedure* for dealing with large unknown initial state errors.
- Case study of fully autonomous multi-robot cooperation, by adding *visual detection* to the leader robot for target tracking, while the other robots follow the leader based on the relative localization.
- Public release of the code to the community. It can be run on off-the-shelf Crazyflie quadrotors by peers for multi-robot applications.

The remainder of this paper is organized as follows. Section II introduces the preliminaries of sensory inputs, the multi-robot model, and the relative localization problem. Section III proposes the fast communication protocol and the relative localization method, following by an observability analysis. Section IV presents the filter initialization method and estimation convergence. Section V discusses distributed formation control, and the self-regulated estimation convergence under unobservable formation control commands. Section VI and Section VII illustrates the simulation and experiment results respectively to verify the effectiveness of the proposed multi-robot localization and control. Section VIII gives the conclusions and discussions.

II. SYSTEM DEFINITION

This section gives definitions of the robot sensory inputs, velocity-based multi-robot kinematic model, and the relative localization problem.

A. Sensory Inputs

For a swarm of robots, essential information for each individual is the relative position of other robots. For clarity of analysis, the model of two arbitrary robots is discussed here, in which robot i needs to estimate the relative position of another robot $\{j \mid j \in \mathbb{N}, j \neq i\}$, where $\mathbb{N} = \{1, 2, \dots, N\}$, and N is the number of robots.

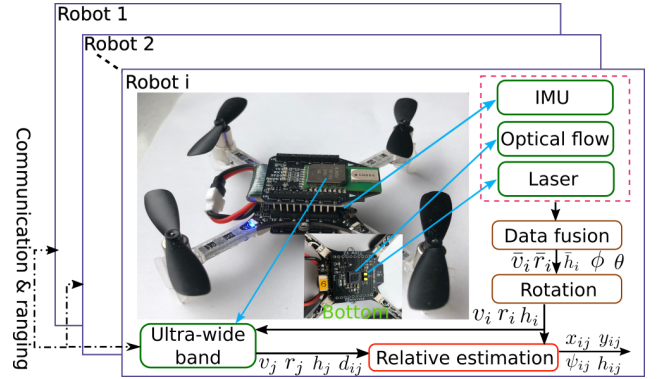


Fig. 2. The scheme of the multi-robot system and all onboard sensors. Specifically, each robot has an inertial measurement unit (IMU), an optical flow sensor, and a downward-pointing laser sensor for obtaining acceleration, rotation rates, velocities, and height. This information is fused by an onboard filter to get the body-frame velocity, yaw rate, and height, which is further rotated to get the horizontal-frame velocity, yaw rate and height. Combined with the other robots' velocity and height information received from communication via the UWB, the relative positions and yaw are estimated.

Before introducing the system model, we define the onboard sensing data as shown in Fig. 2. For each aerial robot, the 3-axis velocity $\bar{v} = [\bar{v}^x, \bar{v}^y, \bar{v}^z]^T$, pitch θ , and roll ϕ attitude in the body frame can be obtained by fusing IMU, height, and optical flow measurements [27]. The yaw rate \bar{r} in the body frame is provided by a gyroscope. The range d_{ij} , meaning the distance between robots i and j , can be measured by ultra wide-band sensors. The variable h is the vertical height calculated from a downward laser measurement \bar{h}_i and the attitude. The final output x_{ij} , y_{ij} , and h_{ij} denote the relative position between the i^{th} and j^{th} robots, which is explained in detail in the following subsection.

B. System Model

In order to make the height comparable among all robots, a horizontal frame with vertical z-axis is introduced for each robot as shown in blue lines in Fig 3.

The 2-axis velocity $\mathbf{v} = [v^x, v^y]^T$ in the inertial horizontal frame for each robot can be obtained from body-frame velocity \bar{v} and the attitude based on the rotation matrix in X-Y rotation sequence, shown as follows:

$$\mathbf{v} = \mathbf{R}_{xy}^{[0:2,0:3]} \bar{v} = \begin{bmatrix} c(\theta) & 0 & s(\theta) \\ s(\phi)s(\theta) & c(\phi) & -c(\theta)s(\phi) \end{bmatrix} \bar{v}, \quad (1)$$

where $\mathbf{R}_{xy}^{[0:2,0:3]}$ means the first two rows of the rotational

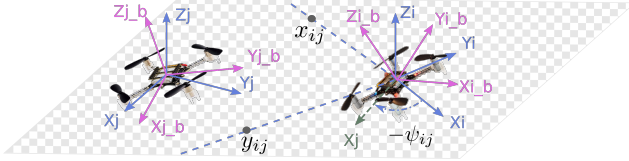


Fig. 3. The diagram of the relative kinematic model, composed by two robots shown in a horizontal plane for simplicity (as they can be at different heights with the relative height h_{ij}). 3D purple axes represent the body frame of each robot, while the 3D blue axes denote the horizontal frame with a vertical z-axis. The relative 2D position $[x_{ij}, y_{ij}]$ and relative yaw ψ_{ij} of j^{th} robot is shown in i^{th} robot horizontal frame in this figure.

matrix \mathbf{R}_{xy} defined by

$$\mathbf{R}_{xy} = \mathbf{R}_x \mathbf{R}_y = \begin{bmatrix} 1 & 0 & 0 \\ 0 & c(\phi) & -s(\phi) \\ 0 & s(\phi) & c(\phi) \end{bmatrix} \begin{bmatrix} c(\theta) & 0 & s(\theta) \\ 0 & 1 & 0 \\ -s(\theta) & 0 & c(\theta) \end{bmatrix}, \quad (2)$$

where $s(\cdot)$, $c(\cdot)$ and $t(\cdot)$ denote $\sin(\cdot)$, $\cos(\cdot)$ and $\tan(\cdot)$, respectively. In addition, according to the relationship between angular velocity vector and angular velocity, the yaw rate r in horizontal frame can be calculated with the 3-axis gyroscope as follows

$$r = \dot{\psi} = -s(\theta)/c(\phi)\bar{p} + c(\theta)/c(\phi)\bar{r} \quad (3)$$

which is derived from another rotation matrix

$$\begin{bmatrix} \dot{\phi} \\ \dot{\theta} \\ \dot{\psi} \end{bmatrix} = \begin{bmatrix} c(\theta) & 0 & s(\theta) \\ s(\theta)t(\phi) & 1 & -c(\theta)t(\phi) \\ -s(\theta)/c(\phi) & 0 & c(\theta)/c(\phi) \end{bmatrix} \begin{bmatrix} \bar{p} \\ \bar{q} \\ \bar{r} \end{bmatrix}, \quad (4)$$

in which \bar{p} , \bar{q} , and \bar{r} are three axis angular velocity in body frame read from the gyroscope.

The filtered vertical height h is communicated directly because of the accurate ranging sensor (VL53L1X). The last sensory input comes from the ultra wide-band, which provides both a distance measurement and a communication ability such as transmitting the velocity, height and yaw rate to other robots. The detailed communication and ranging algorithm will be discussed in the next section.

C. Problem Formulation

Given an arbitrary pair of robots i and j , as shown in Fig. 3, the inputs for estimation are represented by $\mathbf{U}_{ij} = [\mathbf{v}_i^T, r_i, \mathbf{v}_j^T, r_j]^T$. The measurements consist of h_i , h_j and d_{ij} . Define the relative state of j^{th} robot in the i^{th} robot's horizontal frame as $\mathbf{X}_{ij} = [x_{ij}, y_{ij}, \psi_{ij}]^T$, representing 2-axis relative position and the relative yaw as shown in Fig. 3. This relative state is the core problem of this paper and needs to be estimated based on the inputs and measurements.

The kinematic model of the swarm of aerial robots can be derived based on Newton's formulas, and the model takes the transformed velocity and yaw rate as the inputs directly. The continuous model $f(\mathbf{X}_{ij}, \mathbf{U}_{ij})$ is given as

$$\dot{\mathbf{X}}_{ij} = f(\mathbf{X}_{ij}, \mathbf{U}_{ij}) = \begin{bmatrix} R(\psi_{ij})\mathbf{v}_j - \mathbf{v}_i - S r_i \mathbf{p}_{ij} \\ r_j - r_i \end{bmatrix} \quad (5)$$

where $\mathbf{v}_i = [v_i^x, v_i^y]^T$ and $\mathbf{v}_j = [v_j^x, v_j^y]^T$ represent the 2-axis horizontal velocity of two robots; $\mathbf{p}_{ij} = [x_{ij}, y_{ij}]^T$ is a

part of the relative state \mathbf{X}_{ij} meaning 2-axis relative position. $R(\cdot)$ is the rotation function from j^{th} horizontal frame to i^{th} horizontal frame, and S is a skew-symmetric matrix. They are defined as

$$R(\cdot) = \begin{bmatrix} c(\cdot) & -s(\cdot) \\ s(\cdot) & c(\cdot) \end{bmatrix}, \quad S = \begin{bmatrix} 0 & -1 \\ 1 & 0 \end{bmatrix}. \quad (6)$$

Overall, the problem is to estimate the relative state \mathbf{X}_{ij} based on the relative motion model (5), inputs of \mathbf{U}_{ij} , and measurements of h_i , h_j and d_{ij} . Since the height h is accurate, it is used directly for relative position augmentation and height control.

III. FAST COMMUNICATION AND RELATIVE LOCALIZATION

This section gives details of the fast communication protocols, relative state estimation method and the corresponding observability analysis. The two-way-ranging (TWR) communication is extended for bidirectional ranging and signal-loss detection. An EKF is used here for estimation because it is efficient compared to other filters such as the particle filter, and it is more apt to micro-robots which have limited computation power. Lie derivatives are employed to analyze the observability of the system.

A. Fast Communication and Ranging

The two-way-ranging method can provide accurate distance measurements when using UWB with a standard deviation of 0.025m [28]. Instead of communicating with beacons [28], this paper proposes a dynamic recurrent two-way-ranging method, which allows for robust and high-speed communication and ranging between any two flying robots.

The communication design can be divided into high-level topology and low-level protocols. The communication topology, in other words, the multi-robot networks, can be designed arbitrarily since the low-level protocol is independent. In Fig. 4, we give an example of a fully-connected communication network for multiple quadrotors.

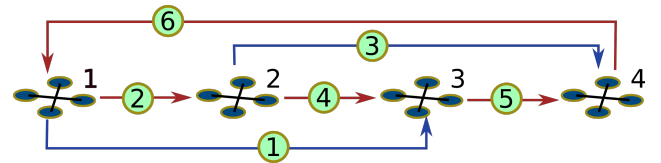


Fig. 4. Communication scheme for multiple robots in an infinite loop. The communication example pertains to 4 robots, starting from the most left robot as the only sender, and following the sequence of the numbers in green circles. Either red line or green line means a low-level communication procedure. However, two robots will swap the sender and receiver mode in red lines, while in green lines the sender will communicate with the next receiver.

Specifically, in this communication loop, all robots are assigned an incremental ID from 1 to N . All robots' UWB modules are set to be in receiver mode except for the 1st robot which is in sender mode at the beginning. Then the 1st robot communicates with robots from $N-1$ to 2, and changes mode into the receiver while the 2nd robot changes into sender mode and starts its own communication. In this

way, the ranging communication can be run on an arbitrary number of robots infinitely with no communication conflicts. Any other communication network can also be achieved by redesigning the communication sequence shown as the red and blue lines in Fig. 4 as long as it is ensured that all robots can communicate without conflicts.

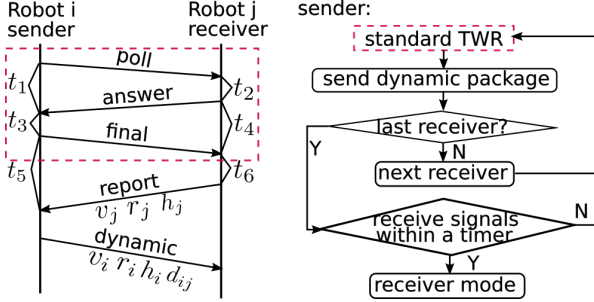


Fig. 5. Left: extended TWR communication, in which an extra ‘dynamic’ chain is designed for bidirectional ranging and communication fault detection. Right: the details of the ‘dynamic’ protocol for fast robust sender-receiver mode transformation by signal detection.

The low-level communication protocol in each line is an extension of TWR method with improvements in bidirectional ranging and dynamic mode changing. The brief review of the standard TWR is shown in the red box in Fig. 5. After three communication steps of ‘poll’, ‘answer’, and ‘final’, the j^{th} robot can calculate the distance d_{ij} based on the signal flight time $t_f = (t_1 t_4 - t_2 t_3) / (t_1 + t_2 + t_3 + t_4)$. With the step ‘report’, the i^{th} robot can also calculate the distance d_{ij} with the flight time $t_f = (t_4 t_5 - t_3 t_6) / (t_3 + t_4 + t_5 + t_6)$. Only the latter flight time is implemented to avoid repeated calculation, and the j^{th} robot can receive the distance value from the i^{th} robot in a new step.

The new extra communication step ‘dynamic’ extends the standard TWR, such that the sender can swap to receiver mode after communication with all other agents. Via this step, the sender sends the distance measurement back to the receiver and checks if it is changing into receiver mode. If the mode swapping succeeds, the high-level communication topology continues with a new sender. Otherwise, the robots retry the swapping procedure. Details are shown in the right diagram which enables robust recurrent communication between multiple robots.

Overall, this extend communication allows undirected ranging among arbitrary multi-robot networks with fast ranging frequency which will be compared with peers’ work in Section VII. This code has been made available.

B. EKF Filter for Relative Localization

We employ the following EKF for state estimation. Based on the standard EKF, its application to the discrete model $F(\hat{\mathbf{X}}_k, \mathbf{U}_k)$ of (5) can be derived as follows.

$$\begin{aligned} \hat{\mathbf{X}}_{k+1|k} &= F(\hat{\mathbf{X}}_k, \mathbf{U}_k) = \hat{\mathbf{X}}_k + \dot{\mathbf{X}}_k \Delta t, \\ \mathbf{P}_{k+1|k} &= \mathbf{A}_k \mathbf{P}_{k|k} \mathbf{A}_k^T + \mathbf{B}_k \mathbf{Q}_k \mathbf{B}_k^T \end{aligned} \quad (7)$$

where Δt is the interval time of updating the Kalman filter, the predicted state is represented by $\hat{\mathbf{X}}_{k+1|k}$, and $\dot{\mathbf{X}}_k$ is the

estimated state at time step k . Furthermore, the first equation in (7) shows the prediction result using the nonlinear model of (5). The second equation denotes the update of error covariance \mathbf{P} caused by the prediction step and input noise covariance \mathbf{Q} . To update \mathbf{P} , the state Jacobian matrix \mathbf{A} and input Jacobian matrix \mathbf{B} are calculated as follows.

$$\begin{aligned} \mathbf{A} &= \frac{\partial F}{\partial \mathbf{X}} = \begin{bmatrix} 1 & r_i \Delta t & (-s(\psi_{ij})v_j^x - c(\psi_{ij})v_j^y) \Delta t \\ -r_i \Delta t & 1 & (c(\psi_{ij})v_j^x - s(\psi_{ij})v_j^y) \Delta t \\ 0 & 0 & 1 \end{bmatrix} \\ \mathbf{B} &= \frac{\partial F}{\partial \mathbf{U}} = \begin{bmatrix} -1 & 0 & y_{ij} & c(\psi_{ij}) & -s(\psi_{ij}) & 0 \\ 0 & -1 & -x_{ij} & s(\psi_{ij}) & c(\psi_{ij}) & 0 \\ 0 & 0 & -1 & 0 & 0 & 1 \end{bmatrix} \end{aligned} \quad (8)$$

After the prediction update, the Kalman filter fuses the predicted state with the observation of the distance between two robots, represented by

$$z = h(\mathbf{X}_{ij}) = \sqrt{\mathbf{p}_{ij}^T \mathbf{p}_{ij}} = \sqrt{x_{ij}^2 + y_{ij}^2 + (h_j - h_i)^2}. \quad (9)$$

Therefore, the Jacobian matrix of observation is

$$\mathbf{H} = \frac{\partial h}{\partial \mathbf{X}} = [x_{ij}/z, y_{ij}/z, 0]. \quad (10)$$

The rest of the Kalman filter process is shown as follows.

$$\begin{aligned} \mathbf{K}_k &= \mathbf{P}_{k|k-1} \mathbf{H}_k^T (\mathbf{H}_k \mathbf{P}_{k|k-1} \mathbf{H}_k^T + \mathbf{R}_k)^{-1}, \\ \hat{\mathbf{X}}_k &= \hat{\mathbf{X}}_{k|k-1} + \mathbf{K}_k (z_k - \mathbf{H}_k \hat{\mathbf{X}}_{k|k-1}), \\ \mathbf{P}_k &= (\mathbf{I} - \mathbf{K}_k \mathbf{H}_k) \mathbf{P}_{k|k-1} \end{aligned} \quad (11)$$

where \mathbf{K} is the Kalman gain. Here, both \mathbf{Q} and \mathbf{R} are noise covariance parameters and can be formulated as diagonal matrices denoted by $\mathbf{Q} = \text{diag}([q_v^2, q_v^2, q_r^2, q_v^2, q_v^2, q_r^2])$ and $\mathbf{R} = \text{diag}([r_d^2])$. q_v , q_r and r_d denote the deviation of the velocity, yaw rate and distance measurements.

C. Observability Analysis

Since the measurement dimension is lower than the state dimension, the system is only observable under some specific robot behaviours. In order to find out and avoid the nonlinear unobservable robot behaviours for more precise estimation, the Lie derivative method is employed here.

From [29], a local weak observability analysis can be performed with model (5) and observation (9). The observability matrix \mathbf{O} is composed by different orders of Lie derivatives.

$$\mathbf{O} = \begin{bmatrix} \nabla \mathcal{L}_f^0 h \\ \nabla \mathcal{L}_f^1 h \\ \nabla \mathcal{L}_f^2 h \end{bmatrix} = \begin{bmatrix} (\partial \mathcal{L}_f^0 h) / (\partial \mathbf{X}) \\ (\partial \mathcal{L}_f^1 h) / (\partial \mathbf{X}) \\ (\partial \mathcal{L}_f^2 h) / (\partial \mathbf{X}) \end{bmatrix} \quad (12)$$

where $\mathcal{L}_f h$ is the Lie derivative of the model function f , and $\nabla \mathcal{L}_f h$ is the differential operator of the Lie derivatives. For simplicity, the power form $\mathbf{p}_{ij}^T \mathbf{p}_{ij} / 2$ is taken as $h(\mathbf{X}_{ij})$ in this subsection. Substitute system model and observation

function, and get

$$\begin{aligned}
\mathcal{L}_f^0 h &= h(\mathbf{X}_{ij}) = \mathbf{p}_{ij}^T \mathbf{p}_{ij} / 2 \\
\nabla \mathcal{L}_f^0 h &= [\mathbf{p}_{ij}^T \ 0] \\
\mathcal{L}_f^1 h &= \nabla \mathcal{L}_f^0 h \cdot f = \mathbf{p}_{ij}^T (R(\psi_{ij}) \mathbf{v}_j - \mathbf{v}_i - S r_i \mathbf{p}_{ij}) \\
\nabla \mathcal{L}_f^1 h &= [(R \mathbf{v}_j - \mathbf{v}_i)^T \ \mathbf{p}_{ij}^T R(\psi_{ij}) S \mathbf{v}_j] \\
\mathcal{L}_f^2 h &= \nabla \mathcal{L}_f^1 h \cdot f = \mathbf{v}_j^T \mathbf{v}_j - 2 \mathbf{v}_i^T R \mathbf{v}_j + \mathbf{v}_i^T \mathbf{v}_i \\
&\quad + \mathbf{v}_i^T S r_i \mathbf{p}_{ij} + \mathbf{p}_{ij}^T R(\psi_{ij}) S \mathbf{v}_j r_i \\
\nabla \mathcal{L}_f^2 h &= [\mathbf{v}_i^T S r_i + r_j \mathbf{v}_j^T S^T R^T \quad -2 \mathbf{v}_i^T R S \mathbf{v}_j - \mathbf{p}_{ij}^T R \mathbf{v}_j r_j]^T
\end{aligned} \tag{13}$$

According to the local weak observability theory, the system is observable only if observability matrix \mathbf{O} is full rank. In other words, the determinant of the matrix in (12) should be non-zero. The determinant is calculated as

$$\begin{aligned}
|\mathbf{O}| &= -\mathbf{p}_{ij}^T R S \mathbf{v}_j (\mathbf{v}_i^T S r_i + r_j \mathbf{v}_j^T S^T R^T) S \mathbf{p}_{ij} \\
&\quad - (2 \mathbf{v}_i^T R S \mathbf{v}_j + \mathbf{p}_{ij}^T R \mathbf{v}_j r_j) (-\mathbf{v}_i^T + \mathbf{v}_j^T R^T) S \mathbf{p}_{ij}
\end{aligned} \tag{14}$$

Although it is difficult to get the full analytical solution of $|\mathbf{O}| \neq 0$, we can extract 3 intuitive and practical unobservable conditions. The first intuitive condition is that $|\mathbf{O}|$ tends to be zero when \mathbf{p}_{ij} is close to zero. This means compact movements of this multi-robot system will cause lower estimation accuracy. The second intuitive unobservable condition is that \mathbf{v}_j cannot be zero, simply because the i^{th} robot cannot find out the heading of j^{th} robot if j^{th} robot is not moving. However, \mathbf{v}_i could be zero according to (14), because the relative state is represented in the body frame of i^{th} robot such that it knows its own heading, even if it is static.

The third unobservable condition concerns the formation behaviour of the multiple robots, in which the relative velocity $-\mathbf{v}_i^T + \mathbf{v}_j^T R^T$ is zero. This will cause the second term of (14) to be zero, and the first term is also zero when yaw rates of both robots remain zero. This is a seriously limiting condition, as this is exactly what happens in most formation flights. The convergence analysis of these unobservable conditions will be discussed in the following sections, and we will then show that the estimation error will remain converged and bounded even if the multi-robot system is under unobservable maneuvers such as the formation flight.

IV. STOCHASTIC INITIALIZATION AND CONVERGENCE ANALYSIS

In this section, an automatic estimation initialization is designed which gives all robots random velocities in finite time, aiming at safe flight and state estimation convergence despite unknown initial states. In addition, the estimation convergence is analyzed.

A. Stochastic Initialization

In practical scenarios, the initial relative states \mathbf{X}_{ij}^0 between robots are usually unknown. Manual measurements of the initial relative position are time-consuming and repeated for each restart of the system, which makes the system less autonomous. Therefore, an automatic initialization method is

designed for all robots to guarantee that the relative states approximate zero before executing the cooperative tasks.

Assumption 1: For simplicity, we assume the control input of the yaw rate for each robot remains zero during the whole flight, i.e., $r_i = r_j = 0$. As the drones are in control of their yaw rates, this assumption can be made true by design.

Based on this assumption, the observability equation of (12) can be reduced to

$$\mathbf{O}_r = \begin{bmatrix} \mathbf{p}_{ij}^T & 0 \\ (R \mathbf{v}_j - \mathbf{v}_i)^T & \mathbf{p}_{ij}^T R(\psi_{ij}) S \mathbf{v}_j \\ \mathbf{0} & -2 \mathbf{v}_i^T R S \mathbf{v}_j \end{bmatrix} \tag{15}$$

The corresponding determinant is reduced to

$$|\mathbf{O}_r| = -2 \mathbf{v}_i^T R S \mathbf{v}_j (-\mathbf{v}_i^T + \mathbf{v}_j^T R^T) S \mathbf{p}_{ij} \tag{16}$$

With this assumption, denote the control inputs for each robot as $\mathbf{u}_i = [v_i^x, v_i^y, r_i]^T$. The initialization inputs are designed as

$$\mathbf{u}_i(t) = \begin{cases} [v_{xR}, v_{yR}, 0]^T, & t \in [2kT, (2k+1)T) \\ -[v_{xR}, v_{yR}, 0]^T, & t \in [(2k+1)T, 2(k+1)T) \end{cases} \tag{17}$$

where v_{xR} and v_{yR} are two-axis velocities generated randomly within the range of $(0, v_{\max}]$ at time $t = 2kT$ in local clocks. Here, $k, v_{\max} = 1m/s$ and $2T$ denote $[0, 1, 2, \dots]$, the maximum velocity and the periodic time interval, respectively. Specifically, each robot does periodical maneuvers, starting with random velocity \mathbf{u}_i in the first time interval T , following by a reversed velocity $-\mathbf{u}_i$ in the second time interval T . The initialization time is set to 30 seconds since this procedure takes 10-30 seconds to converge as shown in the simulation and experiments.

Remark 1: This initialization process prevents the robots from flying away from the initial position in a short time such that a safe flight is guaranteed. In addition, bounded velocities and known time interval T limit the flight radius and furthermore guarantee collision avoidance among multiple robots even if the initial relative positions are unknown, provided that they do not start too close to one another.

B. Convergence of the Initialization Process

This subsection studies the convergence of the proposed initialization process. In view of the observability condition (16) and non-zero velocity inputs (17), the unique unobservable condition is

$$R(\psi_{ij}) \mathbf{v}_j - \mathbf{v}_i = 0, \tag{18}$$

which means both i^{th} and j^{th} robots are flying in same direction with same velocities. Suppose the unobservable situation occurs with probability β over the whole initialization procedure. The convergence analysis for the initialization process can be given as follows for observable and unobservable situations separately.

Theorem 1: If the system input satisfies $R(\psi_{ij}) \mathbf{v}_j - \mathbf{v}_i \neq 0$, all relative states of the Kalman filter are converged and exponentially bounded.

Proof: Observability determinant (16) is not zero when $R(\psi_{ij}) \mathbf{v}_j - \mathbf{v}_i \neq 0$. Therefore, the system satisfies the

nonlinear observability rank condition. According to [30], the corresponding estimator converges exponentially and the estimation error is bounded. The detailed convergence proof is omitted for the weak observable systems as many references have already proved it. ■

Theorem 2: For multiple robots with dynamic estimation model (5), if the control inputs satisfy the initialization process (17) and the unobservable condition (18), then the estimated relative state of the Kalman filter will converge to an unobservable subspace, i.e.

$$\lim_{t \rightarrow \infty} \hat{\mathbf{X}}_{ij}(t) \rightarrow \{x, y, \psi | \sqrt{x^2 + y^2} = z_{\text{GT}}, \psi = \psi_{\text{GT}}\}, \quad (19)$$

and all states $[x_{ij}, y_{ij}, \psi_{ij}]^T$ drift slowly once they reach the subspace. z_{GT} and ψ_{GT} denote the constant distance measurement and constant relative yaw hold by (18).

Proof: From (15), (16) and (18), we can get the observable dimension $\text{Rank}(\mathbf{O}_r) = 2$ in the reduced system. Therefore, the relative estimation system has 2-dimensional weak observability. In order to find the two variables that could be observed and converged based on the Kalman filter, the estimation error is analyzed as follows

$$\tilde{\mathbf{X}}_{ij} = \mathbf{X}_{ij} - \hat{\mathbf{X}}_{ij}. \quad (20)$$

The derivative of the estimate state $\hat{\mathbf{X}}$ can be written as:

$$\dot{\hat{\mathbf{X}}}_{ij} = f(\hat{\mathbf{X}}_{ij}, \mathbf{U}_{ij}) + \mathbf{K}(z - h(\hat{\mathbf{X}}_{ij})). \quad (21)$$

According to [31], the Kalman gain \mathbf{K} and the derivative of the error covariance matrix \mathbf{P} can be represented by

$$\begin{aligned} \mathbf{K} &= \mathbf{P}\mathbf{H}^T\mathbf{R}^{-1} \\ \dot{\mathbf{P}} &= \mathbf{A}\mathbf{P} + \mathbf{P}\mathbf{A}^T - \mathbf{P}\mathbf{H}^T\mathbf{R}^{-1}\mathbf{H}\mathbf{P} + \mathbf{B}\mathbf{Q}\mathbf{B}^T. \end{aligned} \quad (22)$$

Based on the definition of the Kalman function, optimal gain \mathbf{K} always satisfies the following equations.

$$\frac{\partial \text{tr}(\mathbf{P})}{\partial \mathbf{K}} = 0, \quad \mathbf{P} = \text{cov}(\mathbf{X} - \hat{\mathbf{X}}) = \text{cov}(\tilde{\mathbf{X}}) \quad (23)$$

which means that gain \mathbf{K} in (21) can minimize the state error to a transformed subspace. Therefore, if a unique equilibrium space of $\tilde{\mathbf{X}}$ can be found, the relative estimation under the unobservable condition will converge to that space.

The equilibrium space can be found by setting $\dot{\tilde{\mathbf{X}}} = \dot{\mathbf{X}}_{ij} - \dot{\hat{\mathbf{X}}}_{ij}$ to zero. $\dot{\tilde{\mathbf{X}}}_{ij} = [0, 0]^T$ can be derived by combining (5), Assumption 1, and (18). Hence, substitute (21) into $\dot{\tilde{\mathbf{X}}} = -\dot{\hat{\mathbf{X}}}_{ij} = 0$ which yields

$$\begin{bmatrix} R(\hat{\psi}_{ij})\mathbf{v}_j - \mathbf{v}_i \\ 0 \end{bmatrix} + \mathbf{K}(z - h(\hat{\mathbf{X}})) = 0. \quad (24)$$

A two-dimensional time-invariant solution for above equation is

$$\begin{cases} \hat{x}_{ij}^2 + \hat{y}_{ij}^2 = z_{\text{GT}}^2, \\ \hat{\psi}_{ij} = \psi_{\text{GT}}. \end{cases} \quad (25)$$

Here we prove (25) is the unique time-invariant solution by studying all cases. Case 1: $R(\hat{\psi}_{ij})\mathbf{v}_j - \mathbf{v}_i = 0$ and $\mathbf{K} = 0$; case 2: $R(\hat{\psi}_{ij})\mathbf{v}_j - \mathbf{v}_i = 0$ and $z - h(\hat{\mathbf{X}}) = 0$; and case 3:

$R(\hat{\psi}_{ij})\mathbf{v}_j - \mathbf{v}_i \neq 0$ and $\mathbf{K}(z - h(\hat{\mathbf{X}})) \neq 0$, but their sum is zero.

Case 1 holds only if $\mathbf{P}\mathbf{H}^T = 0$ according to (22), which furthermore leads to $\dot{\mathbf{P}} = \mathbf{A}\mathbf{P} + \mathbf{P}\mathbf{A}^T + \mathbf{B}\mathbf{Q}\mathbf{B}^T$. Hence, \mathbf{P} is independent of distance measurement z from (8), while \mathbf{H} is dependent of z from (10). Therefore, $\mathbf{P}\mathbf{H}^T = 0$ does not hold due to the measurement noise. Case 2 corresponds to the time-invariant solution in (25). In case 3, \mathbf{K} is time variant as it contains the integration of state variables which are in matrix \mathbf{A} , \mathbf{B} , and \mathbf{H} according to (22). Thus, this solution is time variant. Therefore, (25) is the unique time-invariant equilibrium state space, and the estimated states will converge to the equilibrium space as shown in (19).

Furthermore, after the relative states reach the equilibrium space, the state update equation in (7) and (11) can be rewritten as

$$\hat{\mathbf{X}}_{k+1} - \hat{\mathbf{X}}_k = \begin{bmatrix} R(\hat{\psi}_{ij})\mathbf{v}_j - \mathbf{v}_i \\ 0 \end{bmatrix} \Delta t + \mathbf{K}_k(z_k - \mathbf{H}_k\hat{\mathbf{X}}_{k-1}) \quad (26)$$

When the state drifts along the circle trajectory $\hat{x}_{ij}^2 + \hat{y}_{ij}^2 = z_{ij}^2$ which still belongs to the equilibrium space, the drift magnitude $\|\hat{\mathbf{X}}_{k+1} - \hat{\mathbf{X}}_k\|$ has a positive correlation to δ_v , δ_z and Δt . δ_v and δ_z denote the upper bound of the Gaussian noise of the velocity and distance measurement. However, the drift speed is slow due to the white noise. ■

Overall, the initialization procedure works mostly under observable conditions because of the random velocity inputs. Therefore, the state has a very small probability β to be converging to the equilibrium space, and $1 - \beta$ to be converging to the correct relative states. Because β is small and state drift is slow in this initialization procedure, states $\hat{\mathbf{X}}$ converge to real values after a finite-time flight.

Remark 2: In the initialization, convergence speed is influenced by the inputs. For example, large velocities keep the observability matrix away from singular points, thus enhancing convergence performance. Besides, the asynchronous nature of the velocity inputs further increases the observability probability and estimation convergence speed.

V. DISTRIBUTED CONTROL AND SELF-REGULATED ESTIMATION CONVERGENCE

This section will discuss the distributed controller design for the multi-robot system based on the aforementioned relative estimation. First, a position error based formation control is proposed. Then, a dynamic inversion controller is designed that can outperform the position-based controller by a feed-forward velocity element. Finally, a type of visual control is proposed for the leader robot such that the swarm of robots can execute tasks fully autonomously.

At the same time, another innovation is presented which proves relative estimation convergence under unobservable motion planning. For example, if the planning command is a formation flight or a hovering formation.

A. Distributed Formation Control

For a formation flight, the reference setpoint is $\bar{\mathbf{p}}_{*i} = [\bar{x}_{*i}, \bar{y}_{*i}]^T$ for the i^{th} robot in the frame of the $*^{\text{th}}$ robot.

For simplicity, $*$ is set to be 1 which means the 1st robot's position is the reference origin. Thus, the desired relative states in each robot's frame can be obtained as

$$\bar{\mathbf{p}}_{i1} = -R(\hat{\psi}_{i1})\bar{\mathbf{p}}_{1i} \quad (27)$$

Therefore, the control error of the relative position is

$$\mathbf{e}_{i1} = \hat{\mathbf{p}}_{i1} - \bar{\mathbf{p}}_{i1} = \hat{\mathbf{p}}_{i1} + R(\hat{\psi}_{i1})\bar{\mathbf{p}}_{1i} \quad (28)$$

where $\hat{\mathbf{p}}_{i1}$ is the relative position estimation. A position error based distributed formation control law for the relative multi-robot systems is designed with constant proportional gain k_p , differential gain k_d , and integral gain k_i as follows

$$\mathbf{v}_i = k_p \mathbf{e}_{i1} + k_d \dot{\mathbf{e}}_{i1} + k_i \int \mathbf{e}_{i1} dt \quad (29)$$

However, position-based control has weak feedback when the position error is small, and this slow response causes control delay. If considering the relative system dynamics

$$\dot{\mathbf{p}}_{ij} = R(\psi_{ij})\mathbf{v}_j - \mathbf{v}_i - Sr_i \mathbf{p}_{ij}, \quad (30)$$

a dynamic inversion formation control law is proposed as follows

$$-k_{DI} \mathbf{e}_{i1} = R(\hat{\psi}_{i1})\mathbf{v}_1 - \mathbf{v}_i - Sr_i \hat{\mathbf{p}}_{i1}. \quad (31)$$

k_{DI} denotes the control gain. Hence, the velocity command for the i^{th} robot is

$$\mathbf{v}_i = k_{DI} \mathbf{e}_{i1} + R(\hat{\psi}_{i1})\mathbf{v}_1 - Sr_i \hat{\mathbf{p}}_{i1} \quad (32)$$

This control law compensates the relative system model thus has quicker tracking performance in all states compared to pure position-based control.

For the formation flight task, each robot should avoid other robots when changing the formation pattern. Therefore, a repulsive velocity is introduced to the system model (30) for collision avoidance.

$$\dot{\mathbf{p}}_{ij} = R(\psi_{ij})\mathbf{v}_j - \mathbf{v}_i - Sr_i \mathbf{p}_{ij} - \alpha \sum_{\substack{m=1 \\ m \neq i}}^N \text{sign}(\mathbf{p}_{im}) \circ |\mathbf{p}_{im}|^{-1} \quad (33)$$

where α is a positive constant which represents the repulsive gain, and the last item in (33) leads to high repulsive velocity when distance is close to avoid collision inter robots. Therefore, the dynamic inversion formation control with collision avoidance is designed as

$$\mathbf{v}_i = k_{DI} \mathbf{e}_{i1} + R(\hat{\psi}_{i1})\mathbf{v}_1 - Sr_i \hat{\mathbf{p}}_{i1} - \alpha \sum_{\substack{m=1 \\ m \neq i}}^N \text{sign}(\mathbf{p}_{im}) \circ |\mathbf{p}_{im}|^{-1}. \quad (34)$$

Lemma 1: Given a formation flight task with the reference states of (27), if estimated state $\hat{\mathbf{X}}$ converges to the real state \mathbf{X} with a small error $\|\hat{\mathbf{X}} - \mathbf{X}\| < \delta_x$, the relative estimation system becomes unobservable.

Proof: Suppose the control gains in (29) or (34) are selected appropriately, such that $\lim \mathbf{e}_{i1} \rightarrow 0$. In addition, from $\|\hat{\mathbf{X}} - \mathbf{X}\| < \delta_x$ we can get that real relative yaw $\psi_{i1} \approx \hat{\psi}_{i1} = C_\psi$ is nearly constant due to assumption of

$r_i = r_1 = 0$. Therefore, the real relative position $\mathbf{p}_{i1} \approx \hat{\mathbf{p}}_{i1} = -\mathbf{e}_{i1} - R(C_\psi)\bar{\mathbf{p}}_{1i}$ approximates to a constant due to the constant formation planning of $\bar{\mathbf{p}}_{1i}$. Therefore, the following equation holds

$$\dot{\mathbf{p}}_{i1} = 0 = R(\psi_{i1})\mathbf{v}_1 - \mathbf{v}_i \quad (35)$$

This leads to a zero determinant in (16) such that the stable states of formation control cause an unobservable condition for the relative estimation system. ■

Remark 3: Notice that this unobservable condition is different from what is discussed in Section IV. Here the unobservable velocity inputs are derived based on correct estimation and formation control, instead of the direct unobservable velocity inputs in the last section. Therefore, the following subsection will give a different proof of the self-regulated estimation stability under the unobservable formation planning.

B. Self-regulated Estimation Convergence

This subsection will give a convergence proof of the relative estimation method under unobservable formation control commands. The idea is that the unobservable conditions caused by formation control inputs are based on correct state estimation. But unobservable conditions will lead to state estimation errors, which result in the change of control commands. Hence, the system is observable again and all states start converging again.

Assumption 2: The estimated relative yaw $\hat{\psi}_{i1}$ can be assumed to approximate the real value ψ_{i1} for a certain time when the system switches to an unobservable condition. This holds because of low-noise yaw rate measurement from the gyroscope and appropriate noise covariance selection for yaw rate in the filter. In addition, this assumption holds also because $\psi = \psi_{GT}$ belongs to the convergence subspace from (19) under unobservable control inputs.

Problem 1: The input and measurement noise is omnidirectional and hence typically has a component orthogonal to the unobservable circle trajectory. This leads to the estimation drift of relative states, hence $\hat{\mathbf{p}} \neq \bar{\mathbf{p}}$.

Theorem 3: Given the converged state estimation \mathbf{p}_{i1} and ψ_{i1} according to Theorem. 2, and the invariant ψ_{i1} in Assumption 2 and the estimation drift in Problem 1. The estimation error will remain converged and bounded even if the multi-robot system is under unobservable maneuvers such as the formation flight.

Proof: First, \mathbf{p} , $\hat{\mathbf{p}}$ and $\bar{\mathbf{p}}$ denote the real value, estimation and control reference of the relative position, respectively. After the initialization and the formation control, relative states satisfy $\mathbf{p} = \hat{\mathbf{p}} = \bar{\mathbf{p}}$. The reference $\bar{\mathbf{p}}$ is constant for a formation flight.

Define the estimation drift in Problem 1 as $\Delta\mathbf{p}$. The incorrect relative estimation has the following relationship to the real and reference relative positions:

$$\hat{\mathbf{p}} = \Delta\mathbf{p} + \mathbf{p} \neq \bar{\mathbf{p}} \quad (36)$$

Substitute (28) into (32), and consider the zero yaw rate in Assumption 1, we can get

$$\mathbf{v}_i = k_{\text{DI}}(\hat{\mathbf{p}}_{i1} - \bar{\mathbf{p}}_{i1}) + R(\hat{\psi}_{i1})\mathbf{v}_1. \quad (37)$$

In view of (35) and (36), the unobservability does not hold due to

$$R(\psi_{i1})\mathbf{v}_1 - \mathbf{v}_i = k_{\text{DI}}(\bar{\mathbf{p}}_{i1} - \hat{\mathbf{p}}_{i1}) \neq 0 \quad (38)$$

Hence, based on Theorem 1, the estimate relative position $\hat{\mathbf{p}}$ will converge to the real value \mathbf{p} .

The system is possibly unobservable during the above procedure, i.e., $\hat{\mathbf{p}} = \bar{\mathbf{p}}$ but $\hat{\mathbf{p}} \neq \mathbf{p}$, which means the relative estimation is incorrect and the system is unobservable. In this case, the relative position will converge to the subspace (the circle trajectory) according to Theorem 2. Furthermore, the incorrect relative estimation $\hat{\mathbf{p}}$ on the subspace can still converge slowly to the correct value \mathbf{p} , because the practical measurement noise on \mathbf{v}_1 and \mathbf{v}_i leads to non-strict zero of $R(\psi_{i1})\mathbf{v}_1 - \mathbf{v}_i$. This result is validated by both simulations and practical experiments.

Remark 4: As for the estimation drift along the unobservable circle path, this problem can be solved by the same analysis in the last paragraph. In addition, the drift to this subspace is slow such that its influence can be neglected.

Overall, no matter what kind of estimation error is introduced, the relative filter and formation control will make the estimation error converge in a self-regulated way with bounded error. ■

C. Visual Control

To give a fully autonomous ability to the aforementioned multi-robot system, a tiny camera is mounted on the leader robot, such that the leader robot can make motion decisions based on the camera input, while the followers fly the same safe path as the leader robot based on the relative estimation and distributed control. Here we study the task of flying multiple robots through a window. The leader needs visual algorithms for detecting the window and creates velocity inputs autonomously, and this function is written as

$$\mathbf{v}_1 = f_{\text{VL}}(\text{Img}, \text{Thr}_u, \text{Thr}_l) \quad (39)$$

where the function input *Img* represents 2D 3-channel RGB image. Thr_u and Thr_l denote the upper and lower color thresholds of the targets. The detailed visual detection and control method f_{VL} is shown in Algorithm 1.

For the follower robots in the vision task, the i^{th} robot creates the velocities based on the states of the $(i-1)^{\text{th}}$ robot, which is written as

$$\mathbf{v}_i = f_{\text{VF}}(\mathbf{v}_{i-1}, \mathbf{p}_{i,i-1}, d_{\text{VF}}) \quad (40)$$

This leader-follower flight of f_{VF} is achieved by setting the reference position as $\bar{\mathbf{p}}_{i-1,i} = d_{\text{VF}}\mathbf{v}_{i-1}/\|\mathbf{v}_{i-1}\|$, which is a constant distance along the reversed velocity direction in the leader's frame. After rotation, the reference position in follower i^{th} robot's frame is $\bar{\mathbf{p}}_{i,i-1} = -R(\hat{\psi}_{i,i-1})\bar{\mathbf{p}}_{i-1,i}$. Therefore, the corresponding velocity for the i^{th} robot can be calculated by position reference $\bar{\mathbf{p}}_{i,i-1}$ and control methods proposed in Section V-A.

Algorithm 1 Visual detection and control on the leader

```

1: procedure  $f_{\text{VL}}(\text{Img}, \text{Thr}_u, \text{Thr}_l)$ 
2:    $flag_{\text{tar}} \leftarrow \text{False}$   $\triangleright$  The flag indicating whether the
   target is detected (true if detected).
3:   while True do
4:      $c_{\text{tar}} = f_{\text{det}}(\text{Img}, \text{Thr}_u, \text{Thr}_l)$   $\triangleright$  Horizontal pixel
   position of the target center from detection function  $f_{\text{det}}$ .
5:      $flag_{\text{tar}} = c_{\text{tar}} \& \text{True}$   $\triangleright$  Update the flag.
6:     if  $flag_{\text{tar}}$  then
7:        $v_1^y = \text{PID}(128/2 - c_{\text{tar}})$   $\triangleright$  Feedback
   control of  $v^y$  to keep the target in the image center. The
   total number of horizontal pixels is configured to 128.
8:        $v_1^x = v_c$   $\triangleright$  A constant forward velocity.
9:        $yaw_o = 0$   $\triangleright$  Set open-loop target yaw to 0.
10:    else
11:       $yaw_o += \text{YI}$   $\triangleright$  Open-loop circle flight with
   incremental yaw  $\text{YI} = 0.04\text{rad}$  in real flights.
12:       $v_1^x = \cos(yaw_o)$ ,  $v_1^y = \sin(yaw_o)$ 
13:    procedure  $f_{\text{det}}(\text{Img}, \text{Thr}_u, \text{Thr}_l)$ 
14:       $x_{\text{hist}}, y_{\text{hist}} \leftarrow \text{histogram}(\text{Img}, \text{Thr}_u, \text{Thr}_l)$   $\triangleright$  2D
   histogram of pixels that belong to the color threshold.
15:       $x_{\text{index}} \leftarrow \text{index}(x_{\text{hist}} > \text{threshold})$   $\triangleright$  Get the
   horizontal index that has pixels over threshold.
16:      if  $\text{size}(x_{\text{index}}) == 2$  then
17:        return  $\text{average}(x_{\text{index}})$ 
18:      else
19:        return 0

```

VI. SIMULATION

In this section, the relative localization method for multiple robots is validated by means of simulation results. The results show the estimation accuracy, convergence performance such as time to convergence, and estimation efficiency in unobservable conditions. Simulation code has been implemented using Python and is available at <https://github.com/shushuai3/multi-robot-localization>

A. Localization Performance

In this simulation, the relative state between two robots is estimated and compared to the ground-truth relative position and yaw to verify the localization accuracy. This simulation is configured with a time interval $dt=0.01\text{s}$ and a maximum moving velocity of 1m/s . The settings of the simulation are: input noise deviation of 0.25m/s and 0.01rad/s , and a distance measurement deviation 0.1m . The initial estimated states are set to zero, while the ground-truth initial states are set randomly and uniformly in a range of $[-3,3]\text{m}$ and $[-1,1]\text{rad}$. The parameters of the relative EKF are set to be $\mathbf{Q} = \text{diag}([0.25^2, 0.25^2, 0.4^2, 0.25^2, 0.25^2, 0.4^2])$, $\mathbf{R} = 0.1^2$, and $\mathbf{P} = \text{diag}([10, 10, 0.1])$, based on the simulated estimation performance.

The robots perform random maneuvers at start-up as explained in Section IV. These allow the filter to converge. Relative localization results are shown in Fig. 6, where we can see that the relative position and yaw approximate the

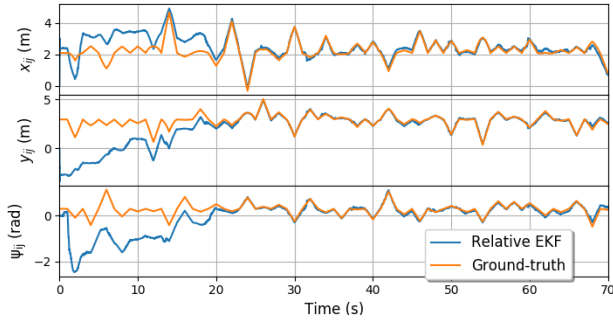


Fig. 6. Simulation results of the relative state estimation between two robots on x_{ij} , y_{ij} , and ψ_{ij} . Both robots are randomly initialized at unknown position and yaw, and they are 2 meter far away each other. Then each robot flies a start-up procedure with 2-second periodic random settings of velocity and yaw rate (1-sec positive velocity and 1-sec negative velocity to guarantee that it flies within 1 meter and not collide with other robots). The orange line represents the ground-truth relative states, while the blue line means the relative states estimated by EKF.

ground-truth after a random flight. As further shown in Fig. 7, this localization with random flight initialization is robust to arbitrary unknown initial states of all robots, and the accuracy will keep high after the convergence. In addition, the localization is stable even if the velocity and yaw rate are randomly time-varying among all robots.

B. Convergence Time

An interesting parameter for our purposes is the expected time to convergence of the estimation. This will dictate how long an initialization maneuver should be before the filter has converged and the swarm can begin to perform coordinated tasks. To evaluate this, we extracted the performance over a set of 50 simulations. These tests are conducted with different random initial position and yaw for each robot, and the inputs of velocity and yaw rate are also randomized.

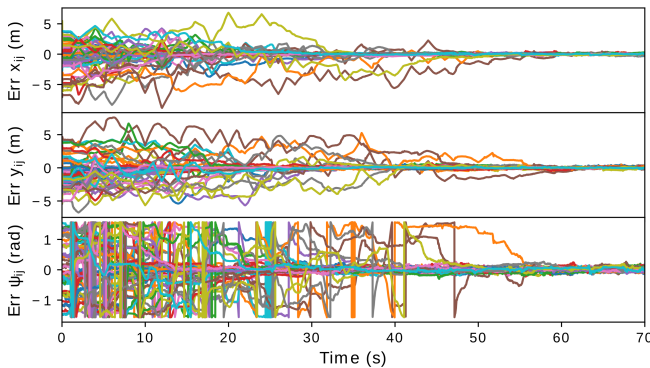


Fig. 7. Simulation results of estimation error convergence. 3 dimensional relative states are shown from 50 tests with different configurations. Each line with different color means different estimation test in three states of x_{ij} , y_{ij} , and ψ_{ij} . All errors are calculated by comparing the estimated states with the ground-truth.

The results are shown in Fig. 7, which shows the relative estimation error. In all 50 different random tests, the errors of three relative states x_{ij} , y_{ij} , and ψ_{ij} tend to be zero after a certain amount of seconds of random flight. The average convergence time is within 20 seconds, while the largest

convergence time is 55 seconds, potentially due to inactive inputs, the initialization being further away from the true initial state, or unobservability-inducing flight behaviours. Overall, the average convergence time is short, and the localization is accurate for multi-robot control.

C. Unobservable Maneuvers and Self-regulated Convergence

In Section III-C, we analytically showed that some flight conditions are unobservable. This subsection will study the influence of unobservable flight behaviour on the relative localization *after* estimation convergence in practice. Two situations that lead to unobservability will be discussed: 1) Formation flight that causes $-v_i^T + v_j^T R^T = 0$, and at same time yaw rates of r_i and r_j remain zero; 2) the j^{th} robot has zero velocity, i.e. $v_j = 0$, where relative yaw ψ_{ij} should be unobservable.

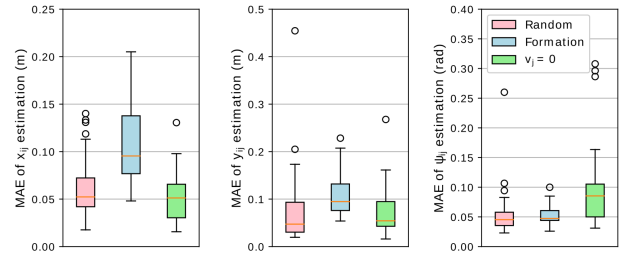


Fig. 8. Error distribution of 3 dimensional relative estimation in different unobservable situations. For each situation, these mean absolute errors (MAE) are obtained from 50 different tests, during the 20 seconds after the estimation convergence. Boxes of red, blue, and green color represent normal random flight, formation flight, and zero velocity of the j^{th} robot, respectively.

In Fig. 8, relative localization performance with unobservability-inducing control inputs are shown. By comparing the red and blue boxes, the influences of formation flight have: 1) an increase of estimation errors on all relative states; 2) the relative estimation is still stable with position error less than 0.2m. This validates the self-regulated estimation convergence theory in Section V-B. The result indicates that once the estimation is not correct, robots will deviate from their role in the formation (in terms of velocity and position), which in turn makes the system observable again. Hence, this unobservability problem is a self-stabilizing phenomenon that operates within acceptable precision bounds as has been discussed in Section V.

In the case that the robot to be localized has zero velocity, the relative yaw estimation has a larger error compared to normal random flight, which can be seen from the green box. However, as indicated in Section III-C, the relative position of x_{ij} and y_{ij} is still observable. Therefore, the green boxes show a similar estimation error with the red boxes in axes of x_{ij} and y_{ij} .

D. Control Performance and Circle Drift

This subsection will present the performance of the proposed distributed control methods. Besides, the state drift on the circle subspace is discussed.

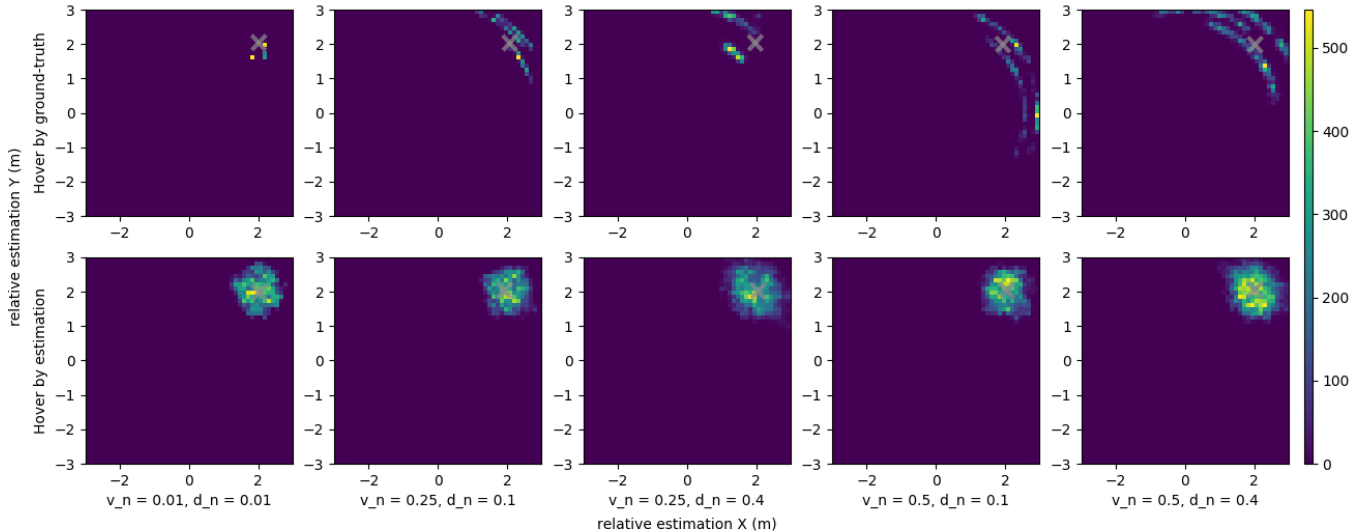


Fig. 9. The relative estimation of absolute hovering and relative hovering with different input and measurement noises. The desired relative position is at (2,2)m shown as a grey cross. Each figure represents the relative trajectories between two robots of 3 tests with 140 seconds for each flight. The first row of absolute hovering means both robots have zero velocity commands irrespective of the estimate of the other drone’s position, while the second row means the second robot keeps a constant relative position with respect to the first robot based on the relative estimation and distributed control.

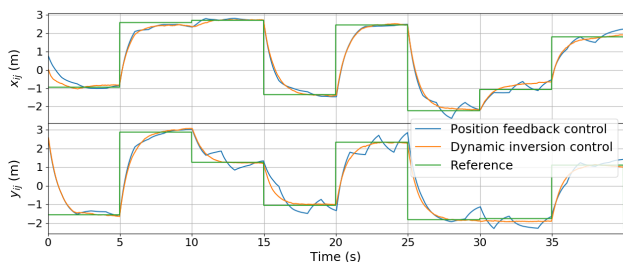


Fig. 10. Formation control performance of position error and dynamic inversion methods for the multi-robot system with delay. The green line shows the reference relative position, the yellow and blue lines show the tracking trajectories of two control methods, respectively.

In Fig. 10, the position error based controller has a larger control error when the position error is small due to delay and less consideration of the system model. However, dynamic inversion control has a quick response time and a small tracking error even when the position error is small. In this comparison, both control methods have the same feedback gain $k = 2$, thus they have similar control performance when the error is large.

To show the extent of the estimation drift along the circle path, Fig. 9 gives two simulation tests, where v_n and d_n denote the velocity input noise and distance measurement noise, respectively. Case 1 on the top row: The drones both hover perfectly with the help of ground truth measurements. The top row shows the estimated relative position by drone 2 under this unobservable condition, with varying amounts of noise. We can conclude that for robots with open-loop unobservable control, the relative estimation tends to drift in the unobservable subspace (the circle trace). The drift error increases when systems have larger noise in velocity and measurement .

Case 2 on the bottom row: Drone 1 at the center perfectly hovers with ground truth, drone 2 uses its estimated relative

position to hover at $\bar{p} = [2m, 2m]$. We can see that the estimation drift will be in a circle area for robots with formation control and constant relative position. Input and measurement noise has less influence on the estimation drift, and the relative estimation keeps stable. Compared case 2 to case 1, we can get that with the same measurement characteristics, the relative estimation error stay bounded if there is distributed control in the bottom row, whereas in the top row the estimates can drift all along the circle. Hence, the self-regulated estimation convergence under distributed control in Section V-B is validate by this simulation result.

VII. REAL-WORLD EXPERIMENTAL RESULTS

Using simulations, we have shown that the filter is capable of converging to correct estimates by means of randomized flight maneuvers, after which it can be effectively used for cooperative flight. This section presents an experimental setup in order to further illustrate the relative estimation efficiency in a real-world multi-robot system. The test scenarios consist of formation flights and autonomous flights based on the monocular camera on the leader robot.

A. Hardware Setup

The swarm of the aerial robot system consists of 5 commercial Crazyflie2 quadrotors. Each quadrotor is equipped with a 3-axis accelerometer, 3-axis gyroscope, flow deck (VL53L1x height sensor and PMW3901 optical flow sensor), and loco deck (DWM1000 ultra wide-band sensor). The flow sensor can provide velocity at 100Hz, and the distance measurement frequency can reach over 333Hz. The processor is an STM32F4 running at 168MHz, on which both relative estimation and control are running.

An OptiTrack motion capture system is used for tracking the ground-truth position and yaw of each robot. The OptiTrack data is only used for post-processing to validate the

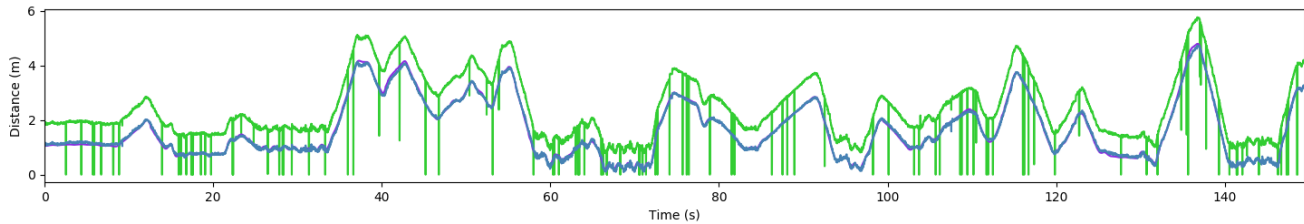


Fig. 11. UWB measurements and data processing. The green line shows the original distance measurements with large outliers. The blue line shows the outlier-rejected and bias compensated distance data. And the purple line is the ground-truth distance from OptiTrack.

relative estimation performance, and has not been used for any other purpose.

B. Data Processing and Communication Performance

The raw ranging measurements from UWB can have outliers and unknown biases. Thus, a median filter is applied to reject the outliers, and a bias function is predetermined by data fitting only once based on the ground-truth distance from OptiTrack.

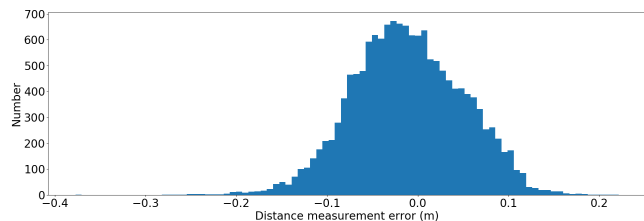


Fig. 12. The distribution of distance measurement errors between the processed distance measurements and ground-truth distance from OptiTrack. These measurements come from a swarm of 3 Crazyflie quadrotors with a 160-seconds flight.

The linear bias fitting function is related to the distance, represented by $b(d_{ij}) = 0.072d_{ij} + 0.62$ where b denotes the ranging bias compared to the ground-truth distance. By median filtering and subtracting the bias, the processed distance is accurate and approximates the ground-truth distance as shown in Fig. 11. In Fig. 12, the distance measurement error between two robots is less than 0.1m and the bias is compensated by the proposed fitting function. This ranging technique has more accurate and less-biased measurements than that in [23].

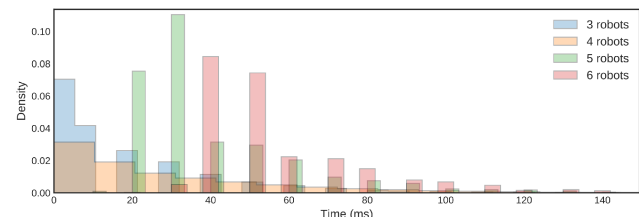


Fig. 13. The distribution of ranging and communication frequency between each two robots with the increase of the number of robots.

Fig. 13 shows the frequency of the proposed communication in Section III-A. As seen from Fig. 13, the ranging frequency of each round decreases with the increase of

the number of robots, but it is still 22Hz for 6 drones to finalize a fully connected ranging topology shown as Fig. 4. For comparison, each ranging measurement takes $1/(22C_6^5) = 0.003s$. Thus, the proposed communication and ranging protocols have higher frequency of 333Hz than 48Hz in [23], 40Hz in [25], and 10Hz in [26].

C. Relative Estimation in Real Experiments

First, the real-world relative estimation performance is shown Fig. 14, which indicates the short convergence time and accurate estimation on real robots. A system with a greater number of robots has a longer convergence time due to the lower frequency of communication and EKF update.

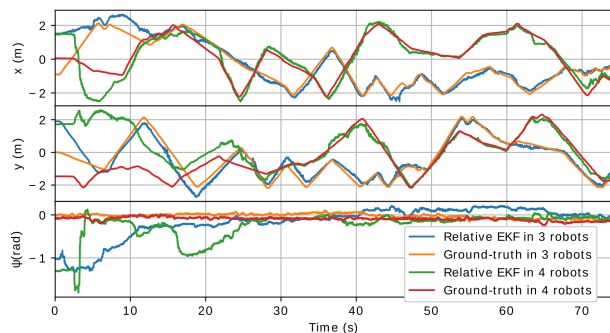


Fig. 14. Real-world relative localization in 3-robot and 4-robot systems respectively. Here, x , y and z denote the absolute XY position and yaw of the 2nd robot, calculated by the relative EKF from the 1st robot, and compared with ground-truth from OptiTrack.

For explicit analysis, the 3-dimensional estimation error is given in the following figure. From Fig. 15, we can see that

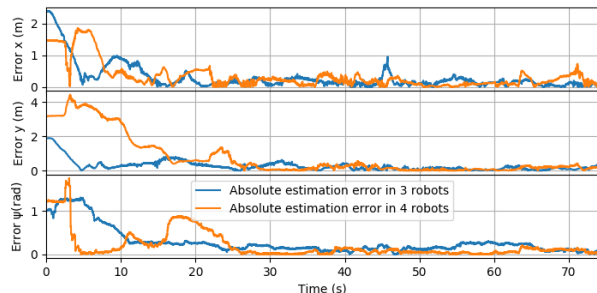


Fig. 15. Absolute error of real-world relative localization in 3-robot and 4-robot systems respectively. Here, x , y and z denote the absolute error of XY position and yaw of the 2nd robot, calculated by the relative EKF from the 1st robot, and compared with ground-truth from OptiTrack.

the unknown initial states can be estimated in 15 seconds for 3 robots and 25 seconds for 4 robots respectively. Less robots need less time for estimation convergence because less robots have higher estimation update and one-round ranging frequency as shown in Fig. 13. After convergence, the absolute estimation errors remain converged even if there are large maneuvers among the multiple robots.

D. Formation Flight

This subsection shows the real-world flight for the formation control, following by a leader-follower flight while the leader is equipped with a tiny monocular camera. Both multi-robot experimental flights are based on the proposed relative localization and distributed control methods.

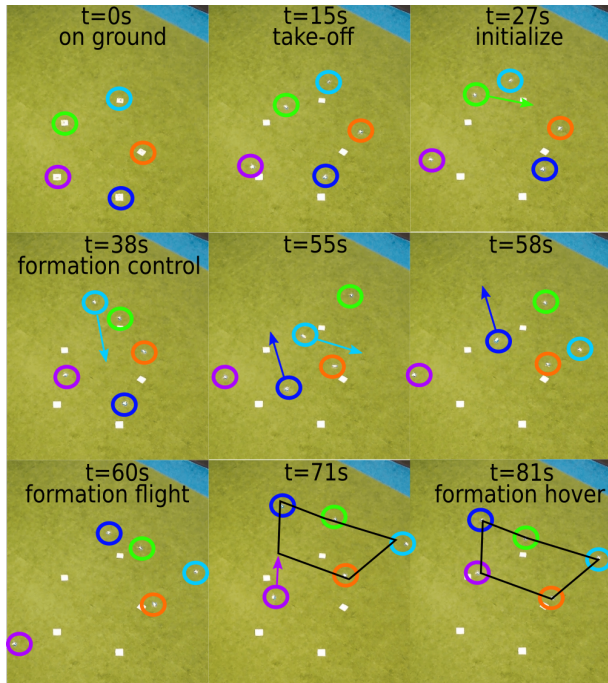


Fig. 16. Top view of the formation flight of 5 robots. Nine figures show different flight status such as take-off, initialization procedure, distributed control for formation flight, and hovering. Five circles with different color show the position of five tiny drones, respectively. Full flight details can be found in the video link https://www.youtube.com/playlist?list=PL_KSX9G0n2P9sgaX3DHnPsBCJ76fLNJ5

Fig. 16 shows how the robot team achieves a formation flight based on the proposed relative localization and distributed control. At $t = 0$ s, all tiny flying robots take off from 5 random unknown positions with unknown random yaw angles. After the 30-seconds initialization procedure, all robots have an accurate relative position and yaw estimation of other robots, and start flying to the desired formation positions with respect to the 1st robot with the orange circle. As seen from the figures at $t = 38$ s, $t = 55$ s, $t = 58$ s, robots with green, blue, and dark blue fly to the desired relative positions which are far away from the initial positions.

Starting from $t = 71$ s all robots did a formation flight with constant relative positions to the 1st robot which keeps a random flight. From the last three figures, we can see the

robot with the purple circle is on the unobservable subspace. Hence, this robot uses a longer time to fly to the desired formation position, which proves the self-regulated estimation convergence under formation control and unobservable subspace due to the velocity noise. Finally, in the right-bottom figure, five robots form an Olympic-flag-like shape. This formation shape is maintained by all robots even at hovering state which is also unobservable for the multi-robot system. Therefore, the proposed control-in-loop relative localization method has consistent convergence in practical experiments even under different unobservable states such as formation flight or hovering.

E. Autonomous Visual Task

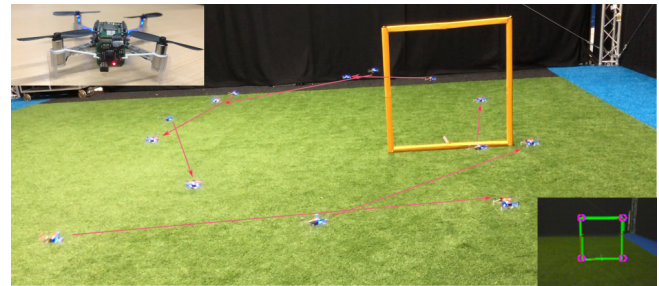


Fig. 17. Experimental results of coordinated leader-follower flight through a window. Two drones connected with a line are captured at a specific time, where the arrow points to the leader. Only the leader drone is equipped with a monocular camera shown in the left-up corner, and the follower robot maneuvers based on the estimated relative position. The window detection results and its four points are shown in the right-down corner.

This part further explores the proposed localization ability for an autonomous task by multiple heterogeneous flying robots. The leader robot is equipped with a tiny camera module (TCM8230MD camera and STM32F4 processor). This enables the 1st robot to detect the four points of the window based on the proposed color filtering and histogram method. The detection result is shown in Fig. 17. Then the leader robot controls its two-axis velocity to move through the center of the window infinitely. At the same time, another robot coordinates with the leader robot in order to fly through the window. As seen in Fig. 17, the follower robot has stable following behaviour with respect to the leader robot, and flies through the window without having a camera only based on the relative localization. In a real-world application, these follower robots could be equipped with different gas sensors (one robot with a CO-sensor, the other with a CH₄ sensor, etc.).

VIII. CONCLUSIONS

This paper proposes a relative localization method and applies it to a swarm of micro flying robots without using any external system or magnetometer. The general multi-robot kinematic model and open-source fast protocols are provided. A novel initialization procedure is proposed and different controllers are designed, along with estimation convergence analysis. In addition, a self-regulated estimation convergence is found and proved for the control-in-loop

multi-robot system even under unobservable control inputs. The relative localization speed and accuracy are verified in both simulation and experimental results. Finally, multi-robot tasks are tested in this swarm system, including formation flight and coordinated window fly-through of multiple robots with only onboard resources. Future work could include the development of an optimal initialization for this relative state estimation, in order to reduce the convergence time.

REFERENCES

- [1] Q. Lindsey, D. Mellinger, and V. Kumar, "Construction of cubic structures with quadrotor teams," *Proc. Robotics: Science & Systems VII*, 2011.
- [2] R. Ritz, M. W. Müller, M. Hehn, and R. D'Andrea, "Cooperative quadcopter ball throwing and catching," in *2012 IEEE/RSJ International Conference on Intelligent Robots and Systems*. IEEE, 2012, pp. 4972–4978.
- [3] M. Gassner, T. Cieslewski, and D. Scaramuzza, "Dynamic collaboration without communication: Vision-based cable-suspended load transport with two quadrotors," in *2017 IEEE International Conference on Robotics and Automation (ICRA)*. IEEE, 2017, pp. 5196–5202.
- [4] M. A. Estrada, S. Mintchev, D. L. Christensen, M. R. Cutkosky, and D. Floreano, "Forceful manipulation with micro air vehicles," *Science Robotics*, vol. 3, no. 23, p. eaau6903, 2018.
- [5] K. McGuire, C. De Wagter, K. Tuyls, H. Kappen, and G. de Croon, "Minimal navigation solution for a swarm of tiny flying robots to explore an unknown environment," *Science Robotics*, vol. 4, no. 35, p. eaaw9710, 2019.
- [6] A. Kushleyev, D. Mellinger, C. Powers, and V. Kumar, "Towards a swarm of agile micro quadrotors," *Autonomous Robots*, vol. 35, no. 4, pp. 287–300, 2013.
- [7] J. A. Preiss, W. Honig, G. S. Sukhatme, and N. Ayanian, "Crazyswarm: A large nano-quadcopter swarm," in *2017 IEEE International Conference on Robotics and Automation (ICRA)*. IEEE, 2017, pp. 3299–3304.
- [8] G. Vásárhelyi, C. Virágh, G. Somorjai, T. Nepusz, A. E. Eiben, and T. Vicsek, "Optimized flocking of autonomous drones in confined environments," *Science Robotics*, vol. 3, no. 20, p. eaat3536, 2018.
- [9] X. Dong, B. Yu, Z. Shi, and Y. Zhong, "Time-varying formation control for unmanned aerial vehicles: Theories and applications," *IEEE Transactions on Control Systems Technology*, vol. 23, no. 1, pp. 340–348, 2014.
- [10] M. Hamer and R. D'Andrea, "Self-calibrating ultra-wideband network supporting multi-robot localization," *IEEE Access*, vol. 6, pp. 22 292–22 304, 2018.
- [11] J. Faigl, T. Krajník, J. Chudoba, L. Přeučil, and M. Saska, "Low-cost embedded system for relative localization in robotic swarms," in *2013 IEEE International Conference on Robotics and Automation*. IEEE, 2013, pp. 993–998.
- [12] M. Saska, T. Baca, J. Thomas, J. Chudoba, L. Preucil, T. Krajník, J. Faigl, G. Loianno, and V. Kumar, "System for deployment of groups of unmanned micro aerial vehicles in gps-denied environments using onboard visual relative localization," *Autonomous Robots*, vol. 41, no. 4, pp. 919–944, 2017.
- [13] V. Walter, M. Saska, and A. Franchi, "Fast mutual relative localization of uavs using ultraviolet led markers," in *2018 International Conference on Unmanned Aircraft Systems (ICUAS)*. IEEE, 2018, pp. 1217–1226.
- [14] V. Walter, N. Staub, A. Franchi, and M. Saska, "Uvdar system for visual relative localization with application to leader-follower formations of multirotor uavs," *IEEE Robotics and Automation Letters*, vol. 4, no. 3, pp. 2637–2644, 2019.
- [15] A. Carrio, S. Vemprala, A. Ripoll, S. Saripalli, and P. Campoy, "Drone detection using depth maps," in *2018 IEEE/RSJ International Conference on Intelligent Robots and Systems (IROS)*. IEEE, 2018, pp. 1034–1037.
- [16] F. Schilling, F. Schiano, and D. Floreano, "Vision-based flocking in outdoor environments," *arXiv preprint arXiv:2012.01245*, 2020.
- [17] A. Weinstein, A. Cho, G. Loianno, and V. Kumar, "Visual inertial odometry swarm: An autonomous swarm of vision-based quadrotors," *IEEE Robotics and Automation Letters*, vol. 3, no. 3, pp. 1801–1807, 2018.
- [18] M. Basiri, F. Schill, D. Floreano, and P. U. Lima, "Audio-based localization for swarms of micro air vehicles," in *2014 IEEE international conference on robotics and automation (ICRA)*. IEEE, 2014, pp. 4729–4734.
- [19] J. F. Roberts, T. Stirling, J.-C. Zufferey, and D. Floreano, "3-d relative positioning sensor for indoor flying robots," *Autonomous Robots*, vol. 33, no. 1-2, pp. 5–20, 2012.
- [20] M. Coppola, K. N. McGuire, K. Y. Scheper, and G. C. de Croon, "On-board communication-based relative localization for collision avoidance in micro air vehicle teams," *Autonomous robots*, vol. 42, no. 8, pp. 1787–1805, 2018.
- [21] K. Guo, Z. Qiu, W. Meng, L. Xie, and R. Teo, "Ultra-wideband based cooperative relative localization algorithm and experiments for multiple unmanned aerial vehicles in gps denied environments," *International Journal of Micro Air Vehicles*, vol. 9, no. 3, pp. 169–186, 2017.
- [22] T. Nguyen, Z. Qiu, T. H. Nguyen, M. Cao, and L. Xie, "Distance-based cooperative relative localization for leader-following control of mavs," *IEEE Robotics and Automation Letters*, vol. 4, no. 4, pp. 3641–3648, Oct 2019.
- [23] S. van der Helm, M. Coppola, K. N. McGuire, and G. C. de Croon, "On-board range-based relative localization for micro air vehicles in indoor leader-follower flight," *Autonomous Robots*, pp. 1–27, 2019.
- [24] H. Xu, L. Wang, Y. Zhang, K. Qiu, and S. Shen, "Decentralized visual-inertial-uw-b fusion for relative state estimation of aerial swarm," *arXiv preprint arXiv:2003.05138*, 2020.
- [25] K. Guo, X. Li, and L. Xie, "Ultra-wideband and odometry-based cooperative relative localization with application to multi-uav formation control," *IEEE transactions on cybernetics*, vol. 50, no. 6, pp. 2590–2603, 2019.
- [26] S. Güler, M. Abdelkader, and J. S. Shamma, "Peer-to-peer relative localization of aerial robots with ultrawideband sensors," *IEEE Transactions on Control System Technology*, 2020.
- [27] M. Greiff, "Modelling and control of the crazyflie quadrotor for aggressive and autonomous flight by optical flow driven state estimation," *MSc. Thesis*, 2017.
- [28] M. W. Mueller, M. Hamer, and R. D'Andrea, "Fusing ultra-wideband range measurements with accelerometers and rate gyroscopes for quadcopter state estimation," in *2015 IEEE International Conference on Robotics and Automation (ICRA)*. IEEE, 2015, pp. 1730–1736.
- [29] R. Hermann and A. Krener, "Nonlinear controllability and observability," *IEEE Transactions on automatic control*, vol. 22, no. 5, pp. 728–740, 1977.
- [30] K. Reif, S. Gunther, E. Yaz, and R. Unbehauen, "Stochastic stability of the discrete-time extended kalman filter," *IEEE Transactions on Automatic control*, vol. 44, no. 4, pp. 714–728, 1999.
- [31] K. Reif, F. Sonnemann, and R. Unbehauen, "An ekf-based nonlinear observer with a prescribed degree of stability," *Automatica*, vol. 34, no. 9, pp. 1119–1123, 1998.